

Multiorbital character of the density wave instability in $\text{La}_4\text{Ni}_3\text{O}_{10}$

Abhi Suthar,¹ Vignesh Sundaramurthy,¹ Matías Bejas,² Congcong Le,³ Pascal Puphal,¹ Pablo Sosa-Lizama,¹ Armin Schulz,¹ Jürgen Nuss,¹ Masahiko Isobe,¹ Peter A. van Aken,¹ Y. Eren Suyolcu,¹ Matteo Minola,¹ Andreas P. Schnyder,¹ Xianxin Wu,⁴ Bernhard Keimer,¹ Giniyat Khaliullin,¹ Andrés Greco,^{2,*} and Matthias Hepting^{1,†}

¹*Max-Planck-Institute for Solid State Research, Heisenbergstraße 1, 70569 Stuttgart, Germany*

²*Facultad de Ciencias Exactas, Ingeniería y Agrimensura and Instituto de Física Rosario (UNR-CONICET), Avenida Pellegrini 250, 2000 Rosario, Argentina*

³*RIKEN Interdisciplinary Theoretical and Mathematical Sciences (iTHEMS), Wako, Saitama 351-0198, Japan*

⁴*Institute of Theoretical Physics, Chinese Academy of Sciences, Beijing 100190, China*

(Dated: August 11, 2025)

Ruddlesden-Popper nickelates exhibit high-temperature superconductivity closely intertwined with charge and spin density wave order. However, fundamental questions persist regarding the interplay between the associated density wave (DW) fluctuations and superconductivity, as well as the orbital character and symmetry underlying the DW instabilities. Here we utilize polarized Raman scattering to investigate the phononic and electronic Raman responses of the trilayer nickelate $\text{La}_4\text{Ni}_3\text{O}_{10}$ across its concomitant charge and spin density wave transitions. In addition to distinct phonon anomalies occurring below the transition temperature, we observe a depletion of continuum spectral weight up to 114 meV and a pronounced peak centered at this energy. By combining momentum-selective information from polarized electronic Raman scattering with model calculations involving both $\text{Ni-}3d_{x^2-y^2}$ and $\text{Ni-}3d_{z^2}$ orbitals, we identify 114 meV as the energy scale $2\Delta_{\text{DW}}$ of the DW gap, characterized by incoherent opening and non-mean-field behavior. Furthermore, the model calculations reveal that the corresponding $2\Delta_{\text{DW}}$ peak exhibits a multiorbital origin, thus shedding light on the nature of the DW instabilities in $\text{La}_4\text{Ni}_3\text{O}_{10}$.

Unconventional superconductors, including cuprates, iron pnictides, and heavy-fermion materials, feature a rich variety of symmetry-broken phases, fluctuations, and electronic instabilities, such as spin and charge density waves, nematicity, pseudogap and strange-metal phenomena, some of which either compete with or facilitate superconductivity [1–6]. Many of the critical insights into these phases and their intertwined character have been obtained using spectroscopic techniques, which probe the associated low-energy excitations [7–14]. In particular, Raman spectroscopy has revealed key characteristics of the interplay between charge, spin, and lattice degrees of freedom in unconventional superconductors, reflected in phonon anomalies, collective electronic modes, spectral weight redistribution and low-frequency scaling behavior of the electronic continuum [15–22].

Recently, Ni-based materials, exhibiting either the infinite-layer or the $\text{La}_{n+1}\text{Ni}_n\text{O}_{3n+1}$ Ruddlesden-Popper (RP) crystal structure, have emerged as a distinct class of unconventional superconductors [23, 24]. For RP nickelates, superconducting transition temperatures (T_c) comparable to those of several cuprate high-temperature superconductors have been reported. Specifically, the bilayer compound $\text{La}_3\text{Ni}_2\text{O}_7$ exhibits superconductivity above 80 K under pressures exceeding 14 GPa [25, 26], while trilayer $\text{La}_4\text{Ni}_3\text{O}_{10}$ was also found to become superconducting under pressure, albeit with lower T_c values between 15 to 40 K [27–30].

At ambient pressure, both $\text{La}_3\text{Ni}_2\text{O}_7$ and $\text{La}_4\text{Ni}_3\text{O}_{10}$

display CDW order [31–35], which is gradually suppressed under pressure before superconductivity emerges [25, 27], suggesting a competitive interplay between these phases. In $\text{La}_4\text{Ni}_3\text{O}_{10}$, a spin density wave (SDW) transition is concomitantly suppressed with the CDW under pressure [34], while residual spin fluctuations that persist in the absence of long-range order might play an essential role for superconductivity, in analogy to the spin-fluctuation mediated pairing in other unconventional superconductors [1]. In $\text{La}_3\text{Ni}_2\text{O}_7$, however, moderate pressure enhances the SDW transition [36], leading to a divergence of the CDW and SDW transition temperatures prior to the onset of superconductivity, suggesting a more complex interplay of electronic phases. More fundamentally, the basic properties of the density-wave (DW) instabilities in $\text{La}_3\text{Ni}_2\text{O}_7$ and $\text{La}_4\text{Ni}_3\text{O}_{10}$ are still under debate—including the size of the DW gaps, their momentum dependence, and the orbital character of the involved electronic states—further complicating efforts to determine how the DW orders intertwine with superconductivity.

For $\text{La}_4\text{Ni}_3\text{O}_{10}$, band structure calculations predict a multiorbital Fermi surface (FS) comprising several dispersive bands with mixed $\text{Ni-}3d_{x^2-y^2}$ and $3d_{z^2}$ orbital character along with a flat band of primarily d_{z^2} character (γ band) [37–47]. Angle-resolved photoemission spectroscopy (ARPES) studies observed a comparable FS topology and proposed direct involvement of d_{z^2} electronic states of the γ band in the formation of the DW, since the γ band crosses the Fermi level (E_F) for temperatures above the density-wave transition $T_{\text{DW}} \approx 140$ K, whereas it drops to 20 meV below E_F for lower temperatures [48]. A different ARPES experiment, however,

* agrec@fceia.unr.edu.ar

† hepting@fkf.mpg.de

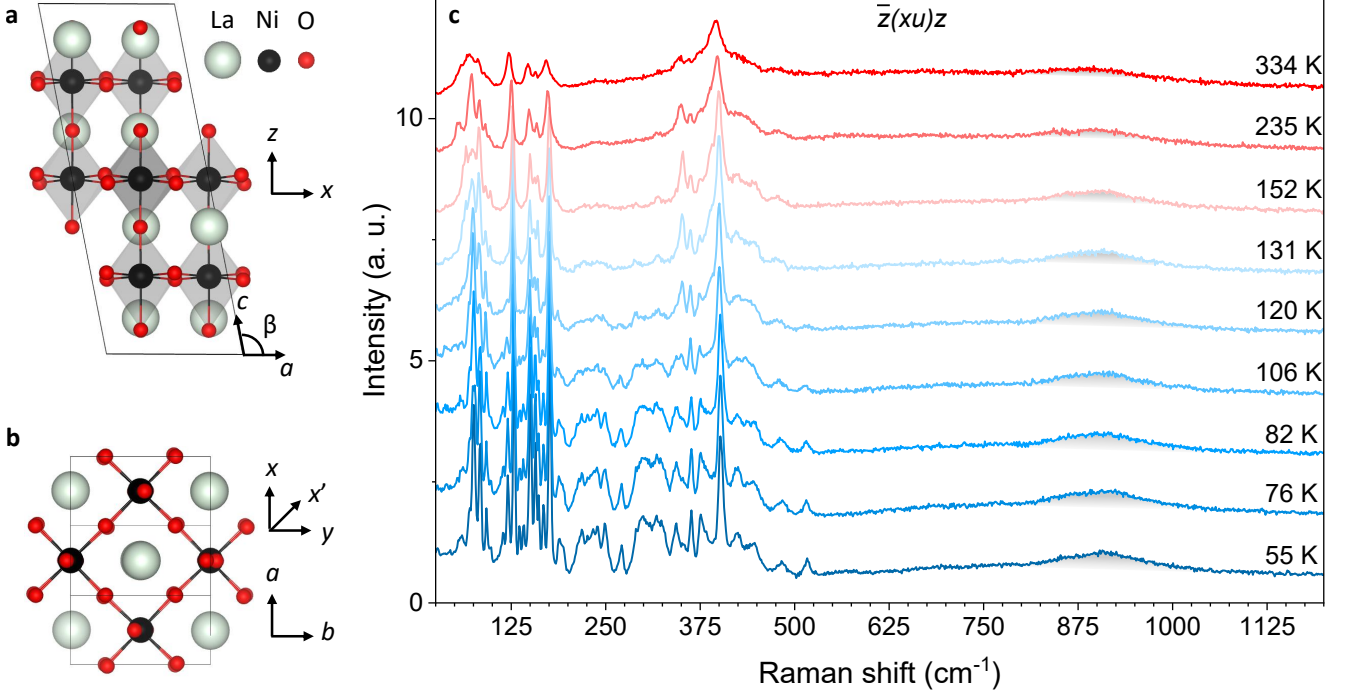


FIG. 1. **Crystal structure and temperature dependence of Raman scattering in $\text{La}_4\text{Ni}_3\text{O}_{10}$.** **a** Side view of the $P2_1/a$ unit cell of $\text{La}_4\text{Ni}_3\text{O}_{10}$, with the monoclinic angle β between the a and c axes indicated. The x and z directions of the laboratory frame of the Raman experiment are also indicated. **b** Top view of the unit cell, with the a and b axes indicated, along with the x , x' , and z directions of the laboratory frame. **c** Raman spectra at various temperatures, acquired in $\bar{z}(xu)z$ scattering configuration (without analyzer). Spectra above (below) the DW transition are colored in red (blue). All spectra are divided by the Bose-Einstein factor and offset in vertical direction by 1.25 a.u. for clarity.

reported that the γ band remains below E_F for temperatures both above and below T_{DW} , while a 12 meV DW gap opens within hybridized $d_{x^2-y^2}$ and d_{z^2} states [49]. Infrared and ultrafast optical spectroscopy as well as scanning tunneling microscopy (STM) studies also reported conflicting DW gap magnitudes [33, 50], with values as large as $2\Delta_{\text{DW}} \approx 122$ meV [51, 52]. A recent Raman spectroscopy study extracted a gap value of $2\Delta_{\text{DW}} \approx 110$ meV and proposed that $d_{x^2-y^2}$ states drive the DW order [53], although this appears to be at odds with a growing body of works emphasizing that the key electronic instabilities and fluctuations in both $\text{La}_4\text{Ni}_3\text{O}_{10}$ and $\text{La}_3\text{Ni}_2\text{O}_7$ involve d_{z^2} or mixed $d_{x^2-y^2}/d_{z^2}$ states [37–39, 41, 46, 47, 54–60].

In this work, we use polarization-resolved Raman scattering to investigate the DW order in high-quality $\text{La}_4\text{Ni}_3\text{O}_{10}$ single crystals. In the phonon sector, we observe several spectral anomalies that carry fingerprints of the DW transition. In particular, high-energy oxygen bond-stretching modes, identified via density functional theory (DFT) based phonon calculations, show clear intensity changes across T_{DW} , whereas frequency and linewidth renormalizations are subtle. The phonon

lineshapes of both low-energy Ni-O bending and high-energy oxygen bond-stretching modes are symmetric, indicating modest coupling between zone-center modes and the electronic continuum, both above and below T_{DW} . The absence of strong frequency and linewidth anomalies as well as asymmetric lineshapes, corroborate the notion that electron-phonon coupling is weak to modest in $\text{La}_4\text{Ni}_3\text{O}_{10}$ [61], suggesting that the DW order is primarily driven by electronic instabilities of the FS rather than electron-lattice interactions.

In electronic Raman scattering, we detect a depletion of continuum spectral weight with decreasing temperature, indicative of a gap opening with $2\Delta_{\text{DW}} \approx 114$ meV, broadly consistent with previous Raman [53] and optical conductivity results on $\text{La}_4\text{Ni}_3\text{O}_{10}$ [51, 52]. Importantly, however, we observe a distinct polarization-dependent peak centered at 114 meV, delineating DW-related effects in the spectra from a nearly flat higher-energy background. Utilizing a two-orbital model for Raman response calculations, we attribute the 114 meV feature to the $2\Delta_{\text{DW}}$ peak of $\text{La}_4\text{Ni}_3\text{O}_{10}$ and establish a mixed Ni- $d_{x^2-y^2}$ and d_{z^2} origin of DW order. In addition, we unveil non-BCS-like behavior of the gap opening and persisting

short-ranged DW correlations above T_{DW} , and discuss possible implications of the multiorbital DW fluctuations for models of superconductivity in RP nickelates.

RESULTS

Samples

High-quality $\text{La}_4\text{Ni}_3\text{O}_{10}$ single crystals were grown using the optical floating-zone method and post-annealed in oxygen atmosphere to optimize oxygen stoichiometry. Single-crystal x-ray diffraction (SXRD) revealed the monoclinic $P2_1/a$ structure (space group no. 14) (Fig. 1a,b). A magnetic transition was observed in susceptibility measurements at $T \approx 140$ K. Details about the sample synthesis and characterization are given in Supplementary Note 1. Phase purity and trilayer stacking in the $\text{La}_4\text{Ni}_3\text{O}_{10}$ crystals was confirmed by scanning transmission electron microscopy (see Supplementary Note 2).

The transition temperature $T_{\text{DW}} \approx 140$ K is consistent with several previous reports of the concomitant SDW and CDW ordering in monoclinic $\text{La}_4\text{Ni}_3\text{O}_{10}$ [31–35], where neutron diffraction established that the SDW emerges in the outer NiO_6 layers of the trilayer block, while SXRD indicated that the CDW modulation occurs in each of the three layers [31]. In transport measurements on crystals from the same batch used for this Raman study, a resistivity downturn with an onset at ~ 15 K was observed for pressures above ~ 20 GPa (to be published elsewhere), suggesting that our crystals exhibit high-pressure superconductivity consistent with $\text{La}_4\text{Ni}_3\text{O}_{10}$ samples in Refs. [27–30]. By contrast, for an orthorhombic variant, which likely corresponds to heavily oxygen-deficient $\text{La}_4\text{Ni}_3\text{O}_{10-\delta}$, the DW transition temperature deviates from 140 K [62, 63], and a tetragonal variant showed neither a DW transition at ambient pressure nor superconductivity under high pressure [64].

Phononic Raman scattering

$\text{La}_4\text{Ni}_3\text{O}_{10}$ in the monoclinic $P2_1/a$ space group (C_{2h} point group) exhibits 99 vibrational modes at the Γ point, out of which 51 are infrared active ($26 A_u + 25 B_u$) and 48 are Raman active ($24 A_g + 24 B_g$). The corresponding Raman tensors are given in Supplementary Note 3. The relation between the x , y , and z directions of the laboratory frame of the Raman experiment and the a , b , and c crystallographic directions is displayed in Fig. 1a,b. Note that the monoclinic angle β introduces an offset of $\sim 11^\circ$ between the c - and z -directions.

Figure 1c provides an initial overview on the temperature dependence of the Raman spectra of a $\text{La}_4\text{Ni}_3\text{O}_{10}$ single crystal. The scattering geometry including the photon polarizations are given in Porto’s notation, where u indicates that no analyzer was inserted in the scattered light path, i.e., $\bar{z}(xu)z$ contains both $\bar{z}(xx)z$ and $\bar{z}(xy)z$

scattering contributions. In the following, we omit the labels \bar{z} and z , denoting the incident and scattered photon directions in backscattering geometry, respectively, for simplicity. Technical details of the Raman experiment are provided in the Methods section.

In the unpolarized (xu) spectrum at 334 K in Fig. 1c, distinct phonon modes appear in the ranges $60\text{--}180\text{ cm}^{-1}$ and $350\text{--}450\text{ cm}^{-1}$, alongside a broad, weak hump centered around 910 cm^{-1} (see shaded area in Fig. 1c). Upon cooling, the phonon linewidths sharpen significantly and several additional modes emerge between 60 and 515 cm^{-1} , while the broad hump shows minor temperature dependence. The most pronounced spectral changes occur between 152 K and 120 K, indicating that the DW transition at $T_{\text{DW}} \approx 140$ K affects the Raman scattering.

For a more detailed analysis, we focus in Fig. 2 on polarized spectra and features below 600 cm^{-1} , which is the typical energy range of phonons in other nickelates [65, 66] and related oxides [15, 67, 68]. Figure 2a,b display Raman spectra in the xx , $x'x'$, xy , and $x'y'$ polarization channels, acquired at 315 and 50 K, respectively. At both temperatures, differences between the xx and $x'x'$ spectra, as well as between the xy and $x'y'$ spectra, are subtle. This is consistent with the relatively small in-plane (orthorhombic) asymmetry between the a and b directions in $\text{La}_4\text{Ni}_3\text{O}_{10}$ (see Supplementary Note 1). By contrast, the difference between spectra in the parallel and cross polarization channels (xx and xy or $x'x'$ and $x'y'$) is striking, with several modes appearing exclusively in one configuration. However, due to the monoclinic angle β of $\text{La}_4\text{Ni}_3\text{O}_{10}$, the diagonal and off-diagonal elements of the Raman tensor mix in our employed backscattering geometry, leading to the appearance of both A_g and B_g modes in each channel.

The detailed temperature dependence and analyses of several representative phonon modes between 355 and 515 cm^{-1} are displayed in Fig. 2c,d. Complementary analyses of lower-energy phonons are presented in Supplementary Note 5. In Fig. 2c, a mode centered around 355 cm^{-1} increases in intensity upon cooling from 334 to 152 K, followed by a strong decrease in intensity for temperatures below T_{DW} (green triangles in Fig. 2c). A mode around 400 cm^{-1} (gray circle in Fig. 2c) continuously sharpens upon cooling from 334 to 55 K, while it retains significant intensity even below T_{DW} . A mode around 515 cm^{-1} (orange squares in Fig. 2d) possesses notable intensity only below T_{DW} whereas it appears to be absent at higher temperatures. The energy, integrated intensity, and linewidth of these three phonons, extracted from fits using Voigt profiles (see Methods), are summarized in Fig. 2e.

In order to assign the phonon modes with these distinct behaviors, we perform density functional theory (DFT)-based structural relaxations of the $P2_1/a$ structure of $\text{La}_4\text{Ni}_3\text{O}_{10}$, followed by phonon frequency calculations using density-functional perturbation theory (DFPT) in combination with the PHONOPY package (see Methods

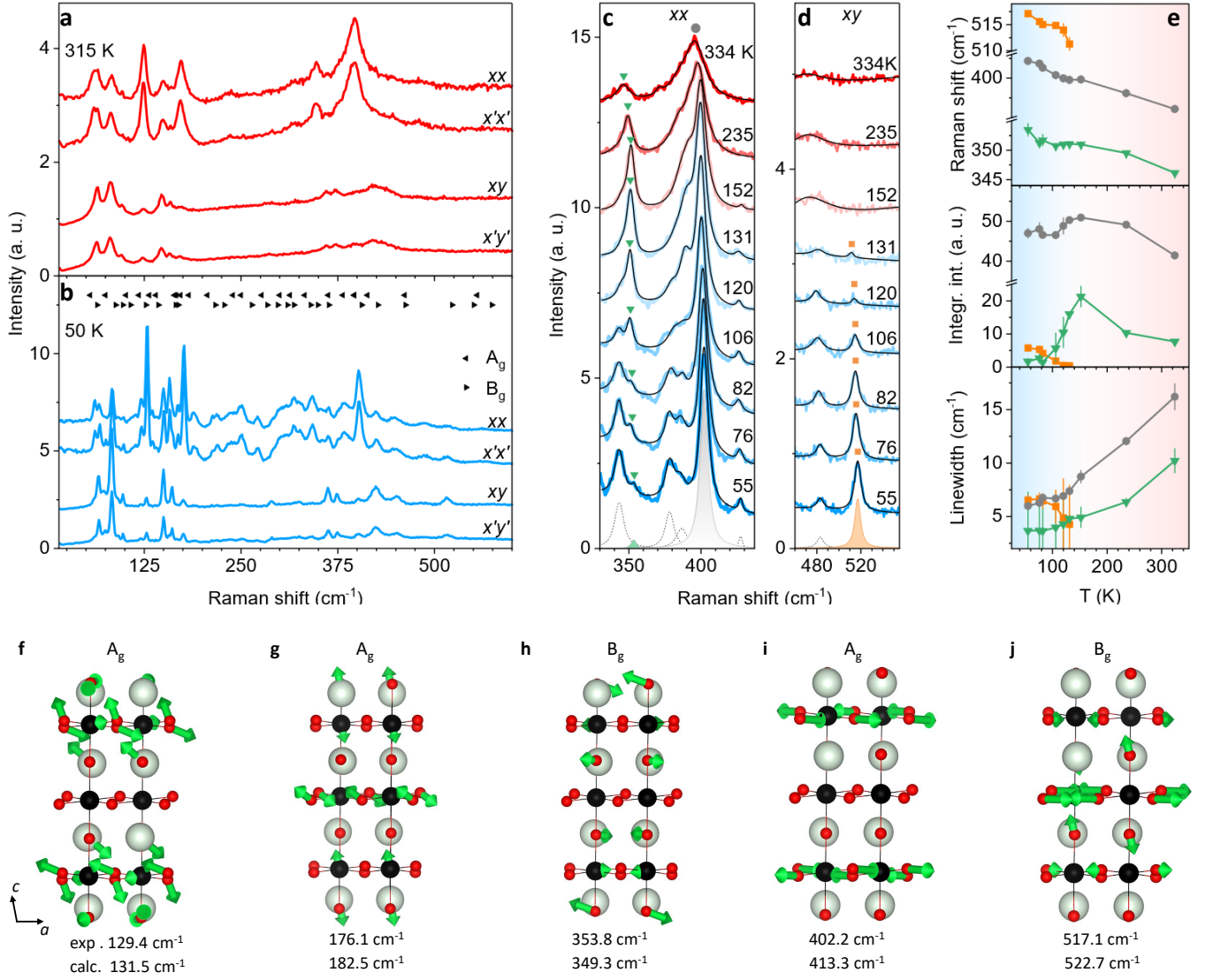


FIG. 2. Phononic Raman scattering in $\text{La}_4\text{Ni}_3\text{O}_{10}$. **a, b** Polarization-resolved Raman spectra at 315 K (**a**) and 50 K (**b**), acquired in xx , $x'x'$, xy , and $x'y'$ scattering configuration, respectively. Black triangles in (**b**) indicate computed phonon frequencies in A_g and B_g symmetry, respectively. **c** Temperature dependence of selected phonon modes in the xx channel. Solid black lines are fits of the data using Voigt profiles. The individual profiles of the 55 K fit are shown as dashed lines at the bottom of the panel. The profiles of phonon modes around 355 and 400 cm^{-1} are highlighted in green and gray, respectively. Green triangles and gray circles indicate the position of the modes at each temperature. **d** Temperature dependence of selected phonon modes in the xy channel. The profile of a phonon mode around 515 cm^{-1} is highlighted in orange, and the orange squares indicate the position of this mode at several temperatures. Spectra in (**a**)-(**d**) are offset in vertical direction by 0.8, 1.8, 1.5, and 0.5 a.u., respectively. **e** Temperature dependence of the energy (top panel), integrated intensity (middle panel), and linewidth (bottom panel), extracted from the fits of the modes indicated by green triangles, gray circles, and orange squares in (**c**) and (**d**). **f-j** Atomic displacement patterns of selected phonon modes. The A_g and B_g mode symmetries are indicated along with the experimentally observed (top) and computed phonon frequencies (bottom). Green arrows indicate the directions and amplitudes of the atomic vibrations. For clarity, only displacements with large amplitudes are shown for each mode. The a and c directions of the $P2_1/a$ unit cell are also indicated.

for details). The computed Raman phonon frequencies are displayed as black triangles in Fig. 2b, and a table of all frequencies is provided in Supplementary Note 4. The computed range, spanning from 55 to 574 cm^{-1} , agrees reasonably well with the range of experimentally observed phonons from 61 to 516 cm^{-1} at 50 K (Fig. 2b).

Note that the $P2_1/a$ symmetry was reported to persist for $\text{La}_4\text{Ni}_3\text{O}_{10}$ below T_{DW} [69, 70], supporting a comparison with the 50 K spectrum and not only the high-temperature spectra.

Figure 2f-j display the atomic displacement patterns of selected phonon modes. We assign a mode prominently

observed at 129.4 cm^{-1} in the xx and $x'x'$ channels in Fig. 2b to an A_g phonon computed at 131.5 cm^{-1} . The mode is characterized by Ni-O bending vibrations in the outer layers of the trilayer unit, along with significant displacements of the La atoms (see green arrows in Fig. 2f). Minor vibrations of the inner Ni-O octahedra are not indicated in Fig. 2f for simplicity. Notably, this mode was identified as a coherent Raman-active phonon that can be excited by ultrashort laser pulses in Ref. [50]. A second prominent phonon in the xx and $x'x'$ channels in Fig. 2b, observed at 176.1 cm^{-1} , likely corresponds to a mode computed at 182.5 cm^{-1} . This mode involves anti-phase motions between the La and Ni atoms in the outer layers, along with bond stretching vibrations of the basal oxygen atoms in the center of the trilayer unit (Fig. 2g). The temperature dependence of the energy, integrated intensity, and linewidth of the 129.4 and 176.1 cm^{-1} phonons extracted from fits are presented in Supplementary Note 5.

A phonon centered at 353.8 cm^{-1} , exhibiting diminishing intensity below T_{DW} (Fig. 2c,e), is assigned to a B_g mode computed at 349.3 cm^{-1} , involving vibrations of the apical oxygen atoms along with displacements of the Ni atoms in the outer Ni-O planes (Fig. 2h). The prominent phonon observed around 402.2 cm^{-1} in Fig. 2c corresponds likely to an A_g mode computed at 413.3 cm^{-1} , involving bond stretching vibrations of basal oxygen in the outer Ni-O planes (Fig. 2i). This vibration pattern is reminiscent of quadrupolar modes in La_2CuO_4 [71, 72], which, unlike the oxygen breathing modes, are insensitive to the on-site Coulomb repulsion U_d of the Cu $3d$ orbitals [71]. Alternatively, the observed phonon might correspond to A_g modes computed at 396.1 or 396.4 cm^{-1} , both of which involve quadrupolar bond-stretching vibrations of the basal oxygen atoms in the inner Ni-O plane. The phonon near 517.1 cm^{-1} , with emergent intensity below T_{DW} in Fig. 2d, matches best with a B_g mode computed at 522.7 cm^{-1} , which is characterized by a breathing distortion of the inner oxygen octahedra (Fig. 2j).

In regions of dense phonon clustering in Fig. 2b, individual modes are difficult to distinguish, especially between 200 and 325 cm^{-1} in the parallel polarization channels. While a high density of phonon modes in this range is consistent with our calculations (see Supplementary Note 4), the overlap of peaks hinders the unambiguous assignment of individual modes.

Electronic Raman scattering

After analyzing the temperature evolution of the phonon sector across the DW transition, we now turn to an extended energy range. In the spectra up to 1750 cm^{-1} in Fig. 3a, a broad peak centered around 910 cm^{-1} emerges most prominently in the xx and $x'x'$ polarization channels. Its linewidth exceeds 150 cm^{-1} even at the lowest measured temperatures, which is sub-

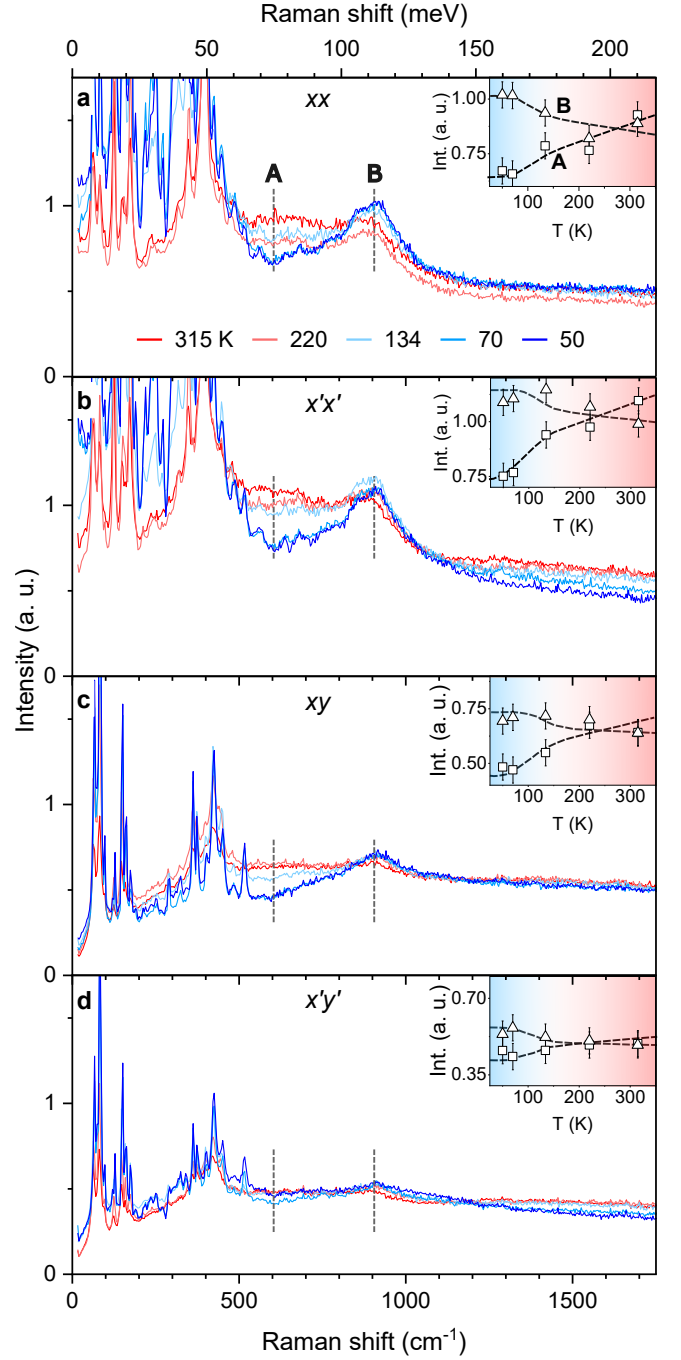


FIG. 3. Electronic Raman scattering in $\text{La}_4\text{Ni}_3\text{O}_{10}$. a-d Raman spectra across a wide energy range, acquired at different temperatures (red to blue lines) in xx , $x'x'$, xy , and $x'y'$ scattering configuration (top to bottom panel), respectively. Vertical dashed lines at 610 cm^{-1} (label A) and 910 cm^{-1} (label B) indicate regions in the spectra with a distinct temperature dependence. The insets show the corresponding temperature dependence (square symbols for A, triangle symbols for B). Dashed lines in the insets serve as a guide to the eye.

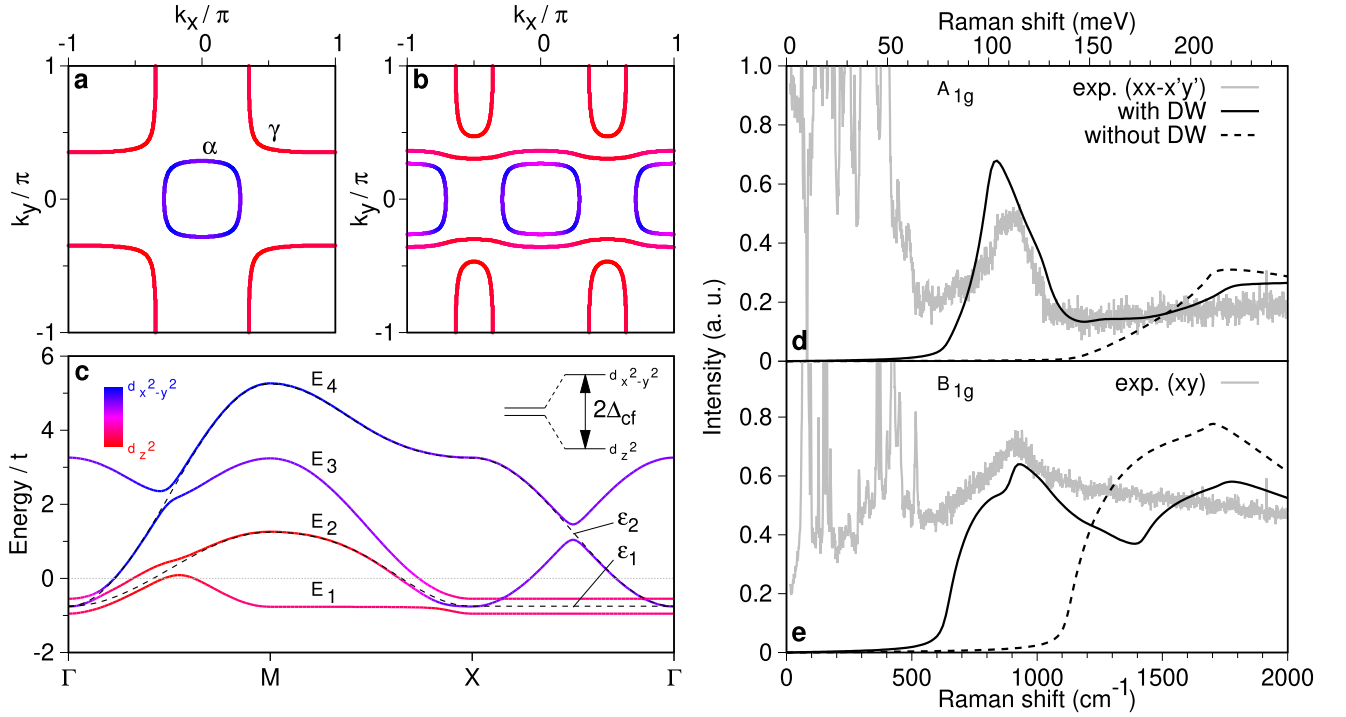


FIG. 4. **Raman response in the two-orbital model with density wave.** **a** Fermi surface in the two-orbital model with α and γ sheets. The color code represents $d_{x^2-y^2}$ (blue), d_{z^2} (red), or mixed (magenta) orbital character. **b** Fermi surface in the presence of an uniaxial DW with $\mathbf{q} = (0, \pi)$ and $\delta = 0.2t$ (see text). **c** Energy bands E_1 to E_4 of the two-orbital model in presence of the DW, with the orbital character resolved according to the color code. For comparison, the bands ε_1 (lower black dashed line) and ε_2 (upper black dashed line) in the absence of a DW are also shown. The inset illustrates the splitting $2\Delta_{cf}$ between the $d_{x^2-y^2}$ and d_{z^2} orbital levels. **d** Raman response in the A_{1g} channel, calculated in the presence (black solid line) and absence of the DW (black dashed line). An energy-dependent quasiparticle weight was applied (see Methods section). Experimental data (gray line) from the $xx - x'y'$ channel are superimposed. **e** Raman response in the B_{1g} channel, calculated in the presence (black solid line) and absence of the DW (black dashed line). Experimental data (gray line) from the xy channel are superimposed.

stantially broader than that of the phonon modes observed up to 515 cm^{-1} . Notably, this feature appears to divide the Raman spectrum into two regimes: a high-energy region that is nearly flat above $\sim 1140 \text{ cm}^{-1}$ and exhibits only weak temperature dependence, and a lower-energy region with strong temperature dependence and regions of either increasing or depleting spectral weight upon cooling. This separation of the Raman spectra in Fig. 3 into distinct energy scales by the 910 cm^{-1} peak suggests that it is likely associated with an electronic excitation rather than multi-phonon scattering. Furthermore, the 910 cm^{-1} peak and a nearly flat background above $\sim 1140 \text{ cm}^{-1}$ is similarly present in Raman spectra acquired with both 632.8 nm (Fig. 3) and 532 nm (see Supplementary Note 5) laser excitation, confirming the robustness of the features.

The insets in Fig. 3a–d display the temperature dependence of the Raman intensity at two representative energies (610 and 910 cm^{-1}) in the four polarization channels. In the xx channel, the intensity at 610 cm^{-1} (label A in Fig. 3a) decreases upon cooling, particularly below T_{DW} . This trend reflects a broader suppression of

spectral weight in the surrounding energy range at least up to 700 cm^{-1} . Below 500 cm^{-1} the detailed behavior of any broad spectral weight distribution is masked by the rapidly growing phonon intensity. Conversely to this spectral weight depletion, the intensity of the 910 cm^{-1} peak (label B in Fig. 3a) increases with decreasing temperature, with the most pronounced enhancement occurring near T_{DW} in the xx channel. The contrasting temperature evolution of features A and B is similarly observed in the other polarization channels (insets in Figs. 3), although it is almost absent in the $x'y'$ channel.

Density wave in a two-orbital model

To gain insights into the origin of the 910 cm^{-1} feature and the temperature-dependent spectral weight at energies lower than 910 cm^{-1} (Figs. 3), we next develop a minimal model to compute the electronic Raman response of $\text{La}_4\text{Ni}_3\text{O}_{10}$. In constructing our model, it is crucial to take into account the multi-band and

multi-orbital nature of $\text{La}_4\text{Ni}_3\text{O}_{10}$, conversely to cuprates which can often be treated as effective single-band systems with a single-sheet $\text{Cu-}d_{x^2-y^2}$ FS [2]. Specifically, first-principles calculations indicate that the active electronic states in $\text{La}_4\text{Ni}_3\text{O}_{10}$ near the Fermi level are composed of $d_{x^2-y^2}$ and d_{z^2} orbitals [37, 38, 73–76], suggesting that at least two orbitals are required to capture the essential low-energy physics and associated electronic excitations. Since both the charge- and spin-density modulations in $\text{La}_4\text{Ni}_3\text{O}_{10}$ occur primarily within the NiO_2 planes [31], we restrict our analysis to a two-dimensional model. In addition, we adopt a simplified fourfold symmetric in-plane geometry for $\text{La}_4\text{Ni}_3\text{O}_{10}$, which allows for a decomposition of the Raman response into the conventional A_{1g} , B_{1g} , and B_{2g} symmetry channels, in analogy to square-lattice cuprates with CuO_2 planes. This approximation is compatible with the observed similarity of the phonon spectra in the xx and $x'x'$ as well as the xy and $x'y'$ channels in Fig. 2a,b, which would not be expected in systems with pronounced orthorhombicity.

We define the model Hamiltonian as $H = H_0 + H_{DW}$, where H_0 describes electrons hopping within and between $d_{x^2-y^2}$ and d_{z^2} orbitals. Details of the model are provided in the Methods section. The crystal field $2\Delta_{\text{cf}}$ splits the e_g orbital manifold into two levels (inset in Fig. 4c), resulting in two dispersive bands ε_1 and ε_2 (black dashed lines in Fig. 4c) and two FS sheets, comprising a circular electronlike pocket with primarily $d_{x^2-y^2}$ and partial d_{z^2} character around Γ , and a holelike pocket of predominantly d_{z^2} character centered at (π, π) (Fig. 4a). Notably, this FS qualitatively reproduces the topology and orbital character reported in ARPES measurements and first-principles calculations for $\text{La}_4\text{Ni}_3\text{O}_{10}$ [37, 38, 48], including the α and γ FS sheets as denoted in Refs. 37 and 38. The β sheet, with its trilayer-induced splitting into β and β' and mixed $d_{x^2-y^2}$ and d_{z^2} character [37, 38], is not implemented in our minimal model.

The term H_{DW} describes a density modulation within the $d_{x^2-y^2}$ and d_{z^2} orbitals, characterized by a wave vector \mathbf{q} and the parameter δ , which modulates the chemical potential to simulate the presence of a DW (see Methods section). We consider a uniaxial density modulation with $\mathbf{q} = (0, \pi)$ and $\delta = 0.2t$, using an effective hopping parameter $t = 0.28$ eV, reflecting effective mass renormalization due to correlations in $\text{La}_4\text{Ni}_3\text{O}_{10}$. The resulting FS is plotted in Fig. 4b and the energy bands E_1 to E_4 , with their orbital character resolved, are displayed in Fig. 4c. Furthermore, we introduce an energy-dependent quasiparticle weight (see Methods section) which effectively reduces the intensities of high-energy interband transition.

Figure 4d shows the computed Raman response in the A_{1g} channel in the presence ($\delta = 0.2t$) and absence ($\delta = 0$) of a DW, respectively. A pronounced peak emerges around 910 cm^{-1} when the DW is present. The B_{1g} response exhibits qualitatively similar behavior, with a DW-induced peak near 910 cm^{-1} of comparable intensity, albeit with a distinct lineshape (Fig. 4e). Consider-

ing a simplified fourfold symmetric in-plane geometry of $\text{La}_4\text{Ni}_3\text{O}_{10}$, with the principal axes aligned along the Ni–O–Ni bond directions rather than the monoclinic setting shown in Fig. 1b, the A_{1g} and B_{1g} channels correspond to the $xx - x'y'$ and xy polarization configurations in Fig. 3, respectively. The corresponding Raman data are overlaid in Fig. 4d,e showing good agreement with the calculated responses.

Notably, in absence of a DW term in our model, the computed Raman response does not exhibit a peak near 910 cm^{-1} in either the A_{1g} or B_{1g} channel in Fig. 4d,e. Instead, only a broad onset with spectral weight from interband transitions appears around 1140 cm^{-1} . Given the values of Δ_{cf} , t , and δ used in our model calculation, a DW gap of $\Delta_{\text{DW}} = 56\text{ meV}$ follows, thus strongly suggesting that the experimentally observed feature around 910 cm^{-1} ($\approx 114\text{ meV}$) originates from the DW and that the gap magnitude of $\text{La}_4\text{Ni}_3\text{O}_{10}$ is $2\Delta_{\text{DW}} \approx 114\text{ meV}$.

In our minimal model, we have not included second-nearest-neighbor hopping t' , which is much smaller than nearest-neighbor hopping t in $\text{La}_4\text{Ni}_3\text{O}_{10}$. The B_{2g} Raman vertex, which scales with t'^2 , is therefore vanishingly small, and a computed $2\Delta_{\text{DW}}$ peak is expected to be minor in the B_{2g} channel, which is consistent with the relatively faint temperature-dependent effects observed for electronic Raman scattering in $x'y'$ polarization in Fig. 3d.

DISCUSSION

Our Raman results in the phonon sector (Fig. 2) reveal that the lattice dynamics of $\text{La}_4\text{Ni}_3\text{O}_{10}$ are affected by the DW transition at $T_{\text{DW}} \approx 140\text{ K}$. Phonon anomalies near T_{DW} were also reported in previous Raman studies [50, 53, 77], although the observed phonon intensity changes in our experiment appear comparatively more pronounced (Fig. 1c and Fig. 2a-e). Moreover, the emergent clusters of densely spaced phonons between 200 and 325 cm^{-1} (see xx and $x'x'$ in Fig. 2b) are not apparent in Ref. [53]. On the other hand, Refs. [53, 77] reported strong phonon peaks at ~ 570 and $\sim 688\text{ cm}^{-1}$, respectively, which are absent in our spectra. In particular, the $\sim 688\text{ cm}^{-1}$ peak is situated far beyond the cut-off frequency of our phonon calculation for $\text{La}_4\text{Ni}_3\text{O}_{10}$ in the monoclinic $P2_1/a$ structure, possibly indicating a deviating structure due to presence of oxygen vacancies and/or intergrown secondary phases, such as other RP or polymorph phases [78, 79], in the samples of Refs. [53, 77]. Orthorhombic [62, 63] and non-superconducting tetragonal [64] variants of $\text{La}_4\text{Ni}_3\text{O}_{10}$ might also exhibit Raman spectra with features deviating from those presented in Fig. 1c and Fig. 2a,b.

Among the most striking fingerprints of the DW transition in the phonon sector is the emergence of new spectral features below T_{DW} , including the mode around 515 cm^{-1} (orange squares in Fig. 2d,e) and the clusters of densely spaced modes between 200 and 325 cm^{-1}

(Fig. 2b). Nevertheless, we refrain from a definitive assignment of the origin of these features to zone-folding induced by the DW, as our DFT-based phonon calculation for the ordinary $P2_1/a$ unit cell already predicts modes at these energies (triangle symbols in Fig. 2b). Instead, the emergence of new modes in our Raman spectra might be attributable to a reduction of metallic screening below the metal-to-metal transition at T_{DW} [31, 48] due to partial FS gapping, rendering previously overdamped $P2_1/a$ phonons observable.

Notably, renormalization effects on the phonon self-energy near T_{DW} , affecting both the real (frequency) and imaginary (linewidth) parts, are relatively subtle in our measurements compared to those observed for zone-center phonons of canonical DW systems [80]. Specifically, the linewidth narrowing with decreasing temperature of the phonons at 355 and 400 cm^{-1} (Fig. 2e, bottom panel) is consistent with anharmonic phonon decay without influence from a phase transition, and slight anomalies near T_{DW} in our data remain within the experimental error bars. For the phonon frequencies (Fig. 2e, top panel), we observe a subtle yet statistically significant dip below T_{DW} , interrupting an otherwise monotonic trend of anharmonic hardening. A similar dip in the frequency evolution below T_{DW} occurs also for the low-energy bending modes at 129 and 176 cm^{-1} (see Supplementary Note 5), involving La, Ni, and O displacements. While we cannot rule out that the frequency dip primarily originates from a change of electron-phonon coupling across T_{DW} , the faint softening of various low- and high-energy modes, together with the diminishing of intensity of a few specific modes (orange squares in Fig. 2d,e), more likely reflects subtle structural changes across T_{DW} , such as b -axis expansion [69] and small variations in octahedral tilt angles, while the $P2_1/a$ symmetry is retained [69, 70].

In this context, we also note that all phonon modes resolved in our spectra exhibit symmetric peak profiles both above and below T_{DW} (Fig. 2a–d and Supplementary Note 5), without any signatures of Fano lineshapes that would signal coupling between a discrete phonon excitation and the electronic continuum [19]. Both the absence of clear renormalization effects on the phonon self-energy near T_{DW} and the lack of Fano lineshapes are consistent with theoretical studies predicting moderate to weak electron-phonon coupling in RP nickelates [69, 81–84]. Furthermore, the absence of clear signatures of electron-phonon coupling in our data aligns with recent inelastic x-ray scattering (IXS) results on $\text{Pr}_4\text{Ni}_3\text{O}_{10}$, where no phonon anomalies were detected at the wavevectors associated with either CDW or SDW order [61], suggesting that electron-phonon interactions may play only a minor role in driving the DW transition. However, our findings stand in contrast to a previous unpolarized Raman study on $\text{La}_4\text{Ni}_3\text{O}_{10}$ powder [77], which proposed a crossover from an electron-phonon coupled high-temperature regime to an electron-electron correlated phase below T_{DW} , based on an asymmetric fit with

a single envelope capturing several overlapping phonons.

A second energy scale in our Raman spectra, extending beyond the phonon sector up to $\sim 114 \text{ meV}$ ($\sim 910 \text{ cm}^{-1}$), is characterized by temperature-dependent continuum spectral weight, with its upper bound marked the DW peak. The distinct electronic Raman responses observed in different polarization channels (Fig. 3) reflect that varying photon polarizations effectively project out different regions of the Brillouin zone. This access to the momentum dependence of DW-related effects complements the information from zone-center phonons and, in combination with the two-orbital model calculations, enables identification of the multiorbital character of the DW instability.

Specifically, Fig. 4d,e illustrate that the calculated $2\Delta_{\text{DW}}$ peaks in the A_{1g} and B_{1g} channels align closely with the experimental data. Importantly, both the calculated A_{1g} and B_{1g} response match the data, without requiring an individual scaling factor for each channel, underscoring the consistency of the model. Irregular lineshapes of the experimentally observed DW peaks are also reproduced by the calculations, in particular the low-energy shoulder around $\sim 95 \text{ meV}$ ($\sim 760 \text{ cm}^{-1}$) in the B_{1g} channel. In complementary calculations, where the Raman vertex accounts exclusively for either $d_{x^2-y^2}$ to $d_{x^2-y^2}$ or d_{z^2} to d_{z^2} transitions, we also obtain irregular lineshapes (see Supplementary Note 6), implying that lineshape features of the $2\Delta_{\text{DW}}$ peak are primarily governed by the Fermi surface topology rather than distinct orbital contributions. However, in the absence of orbital mixing, the calculated relative intensity between the $2\Delta_{\text{DW}}$ peaks in the A_{1g} and B_{1g} channels as well as the linewidths deviate significantly from experiment (see Supplementary Note 6)—a discrepancy that corroborates our assignment of the multiorbital character of the DW. While these results challenge the conclusion of Ref. 53 of a pure $d_{x^2-y^2}$ character of the DW in $\text{La}_4\text{Ni}_3\text{O}_{10}$, they align with several theoretical studies emphasizing that a multiorbital basis is required for modeling the intertwined electronic phases and instabilities in RP nickelates [37–39, 41, 46, 47, 54, 55].

As a key result of our study, the observed position of the $2\Delta_{\text{DW}}$ peak around $\sim 114 \text{ meV}$ clearly marks the energy gap in $\text{La}_4\text{Ni}_3\text{O}_{10}$. This value is comparable to gap magnitudes determined by ultrafast optical spectroscopy on $\text{La}_4\text{Ni}_3\text{O}_{10}$ [51, 52], but deviates substantially from the lower range of reported values, with Δ_{DW} between 12 and 35 meV from ARPES, STM, and a different Raman study [33, 48, 49, 77]. Notably, optical conductivity measurements on bilayer $\text{La}_3\text{Ni}_2\text{O}_7$ extracted $2\Delta_{\text{CDW}} \approx 100 \text{ meV}$ and assigned this gap unambiguously to the CDW, since the two ordering phenomena are disjoint in that material, with $T_{\text{CDW}} \approx 110 \text{ K}$ and $T_{\text{SDW}} \approx 150 \text{ K}$ [85]. The similarity in gap magnitudes suggests that the $\sim 114 \text{ meV}$ gap in $\text{La}_4\text{Ni}_3\text{O}_{10}$ is also associated with the CDW. Given this scenario, the lower-energy features observed in other experiments [48, 49, 77] may correspond to the SDW gap of $\text{La}_4\text{Ni}_3\text{O}_{10}$. In our

spectra, the low-energy region is partially obscured by densely clustered, intense phonons (Fig. 3). However, we note a pronounced enhancement of spectral weight below ~ 50 meV in the $x'x'$ channel below T_{DW} , which warrants targeted investigation in a future high-resolution Raman study to clarify a possible hierarchy of DW-related energy scales.

The temperature dependence of the $2\Delta_{\text{DW}}$ peak at 114 meV and the continuum spectral weight at lower energies exhibit several unconventional characteristics: Although the $2\Delta_{\text{DW}}$ peak gains most spectral weight below T_{DW} (insets in Fig. 3, label B), it is already observable well above the transition temperature. This behavior deviates from expectations based on a BCS mean-field scenario, where both the gap and the associated collective mode should vanish at $T = T_{\text{DW}}$. Instead, the persistence suggests that the CDW amplitude is already finite above T_{DW} , but its correlation length short-ranged and quasi-two-dimensional. In addition, the temperature evolution of the continuum is characterized by a gradual depletion of spectral weight (insets in Fig. 3, label A) rather than a “coherent” opening of the gap, reminiscent of pseudogap phenomena observed in cuprates and other correlated materials [86, 87]. An incoherent gap opening has also been found in optical conductivity measurements on $\text{La}_3\text{Ni}_2\text{O}_7$ [85], as well as in related oxides [68]. Notably, recent Landau theory considerations predict that the CDW is subordinate to the SDW [88], and the small 12 meV gap in $\text{La}_4\text{Ni}_3\text{O}_{10}$ observed in ARPES appears to follow a more conventional BCS-like temperature dependence [49].

Finally, while our two-orbital minimal model is not devised to capture the full complexity of $\text{La}_4\text{Ni}_3\text{O}_{10}$, such as the three-dimensionality of the DW order [48], the presence of four FS sheets [37], and various structural subtleties [62–64], it nonetheless yields several robust and general insights: (i) The identification of the multiorbital character of the DW does not depend sensitively on details of the underlying FS. Specifically, our model considers one electronlike and one holelike pocket, representing the α and γ FS sheets of $\text{La}_4\text{Ni}_3\text{O}_{10}$, with hybridized $d_{x^2-y^2}/d_{z^2}$ and nearly pure d_{z^2} orbital character, respectively. Nevertheless, similar multiorbital DW features in the Raman response can be obtained from a model that mimics the α and a β -like sheet of $\text{La}_4\text{Ni}_3\text{O}_{10}$, given that the β sheet includes at least partial d_{z^2} character (not shown here). (ii) The results are robust against the choice of the exact wave vector of the DW, as long as it connects FS regions with mixed orbital character. (iii) An upper limit for the CDW amplitude in $\text{La}_4\text{Ni}_3\text{O}_{10}$ and related RP nickelates can be estimated. Specifically, we obtain a modulation of ± 0.2 electrons relative to the mean, given that the canonical electron filling $n = 4/3$ and a modulation $\delta = 0.2t$ of the chemical potential yields good agreement with the experimental data in Fig. 4d,e, and assuming that Δ_{CDW} cannot exceed the interband transitions at Γ in a fully coherent-band picture.

CONCLUSION

In summary, our polarization-resolved Raman study uncovers the phononic hallmarks of the DW transition in $\text{La}_4\text{Ni}_3\text{O}_{10}$, including the emergence of modes below T_{DW} , intensity changes of persisting modes, and subtle frequency anomalies. The combination of momentum selectivity of electronic Raman scattering and two-orbital model calculations enables the identification of the $2\Delta_{\text{DW}}$ peak of $\text{La}_4\text{Ni}_3\text{O}_{10}$ and its multiorbital origin, involving both $\text{Ni-}d_{x^2-y^2}$ and d_{z^2} states. Spectral weight within the DW gap of approximately 114 meV depletes incoherently with decreasing temperature, while the $2\Delta_{\text{DW}}$ peak persists even above T_{DW} . The corresponding ratio $2\Delta_{\text{DW}}/k_{\text{B}}T_{\text{DW}}$ exceeds the weak-coupling BCS limit, signaling short-range correlations and a strong-coupling character of the DW instability.

Notably, our results lend strong support to theoretical models of RP nickelates that incorporate multiorbital DW instabilities, particularly those that assign prominent roles to d_{z^2} states [38, 39, 41, 46, 47, 54, 55]. Given that both the orbital character and momentum structure of the hybridized $\text{Ni-}d_{x^2-y^2}/d_{z^2}$ DW correlations identified here in the ordered phase at ambient pressure exhibit close correspondence to the persisting DW fluctuations at high pressure, several constraints on superconducting pairing models can be inferred. Specifically, if these fluctuations either compete with or mediate superconductivity, their finite wavevector and interorbital nature might favor pairing states with sign-changing order parameters between distinct FS sheets, supporting extended s^{\pm} -wave pairing symmetry as a viable candidate [39, 89–91], and strongly motivating future Raman investigations not only of the pressure dependence of the DW phenomenon, but also the potential appearance of a superconducting pair-breaking peak in RP nickelates.

METHODS

Polarized Raman scattering. The Raman experiments were performed with a HORIBA Jobin Yvon LabRAM HR800 spectrometer in backscattering geometry, using a He-Ne laser (wavelength 632.8 nm) focused on the sample with a x50 magnification ultra-long working distance objective. The laser power under the microscope was less than 1 mW to minimize heating effects on the sample. The temperatures indicated in the figures of the main text were determined by Stokes/anti-Stokes intensity analysis. All plotted Raman spectra were divided by the Bose-Einstein factor. An ultra-low frequency filter (consisting of two volume Bragg-grating filters) was used to suppress elastically scattered light. For the low-temperature measurements, a KONTI helium-flow cryostat from CryoVac was used.

The Raman spectra in Fig. 2c,d were fitted to a superposition of Voigt profiles resulting from a convolution of the intrinsic Lorentzian lineshape with the Gaussian spectrometer resolution, determined as 2 cm^{-1} from the spectrum of a Ne gas discharge lamp. For the background in the fits of Fig. 2c,d, hyperbola and linear functions were used, respectively.

Phonon calculations. The calculations were performed using density functional theory (DFT) as implemented in the Vienna *ab-initio* simulation package (VASP) code [92]. The Perdew–Burke–Ernzerhof (PBE) [93] exchange–correlation functional and the projector-augmented-wave (PAW) [94] approach were used. Lattice constants and internal atomic positions were relaxed with GGA, with an plane-wave cutoff energy of 600 eV. Forces were minimized to less than 0.001 eV/Å in the relaxation. The relaxed structural parameters were $a = 5.429330\text{ Å}$, $b = 5.50095\text{ Å}$, and $c = 14.20531\text{ Å}$.

In the phonon calculations, the cutoff energy was set to 400 eV for expanding the wave functions into plane-wave basis, and the number of k points was set to $3 \times 4 \times 4$ for a $1 \times 2 \times 2$ supercell. The real-space force constants of the supercells were calculated using density-functional perturbation theory (DFPT) [95] and the phonon frequencies were calculated from the force constants using the PHONOPY code [96, 97]. A table of the resulting Raman phonon frequencies is provided in Supplementary Note 4.

Two-orbital model. The minimal model with two orbitals is defined as $H = H_0 + H_{DW}$, where the bare model without DW modulation is given by $H_0 = \psi_{\mathbf{k}}^\dagger H_{\mathbf{k}} \psi_{\mathbf{k}}$, with $\psi_{\mathbf{k}}^\dagger = (x_{\mathbf{k}}^\dagger, z_{\mathbf{k}}^\dagger)$ and $x_{\mathbf{k}}^\dagger$ ($z_{\mathbf{k}}^\dagger$) denoting the creation operator for an electron in the $d_{x^2-y^2}$ (d_{z^2}) orbital. The 2×2 matrix $H_{\mathbf{k}}$ is the Hamiltonian in the orbital basis, with

$$H_{\mathbf{k}} = \begin{bmatrix} t_{xx} & t_{xz} \\ t_{xz} & t_{zz} \end{bmatrix} \quad (1)$$

where the element $t_{xx} = -\frac{3}{2}t(\cos k_x + \cos k_y) + \Delta_{\text{cf}} - \mu$ describes hopping between $d_{x^2-y^2}$ orbitals, $t_{zz} =$

$-\frac{1}{2}t(\cos k_x + \cos k_y) - \Delta_{\text{cf}} - \mu$ corresponds to hopping between d_{z^2} orbitals, and $t_{xz} = \frac{\sqrt{3}}{2}t(\cos k_x - \cos k_y)$ accounts for hopping between the $d_{x^2-y^2}$ and d_{z^2} orbitals. The crystal field splitting of the e_g orbital levels is denoted by Δ_{cf} , μ is the chemical potential, and \mathbf{k} is the momentum in a 2D square-lattice.

The Hamiltonian in the band basis is diagonal

$$H_{\mathbf{k}}^B = \begin{bmatrix} \varepsilon_1 & 0 \\ 0 & \varepsilon_2 \end{bmatrix} \quad (2)$$

where $\varepsilon_1 = (t_{xx} + t_{zz})/2 + r$ and $\varepsilon_2 = (t_{xx} + t_{zz})/2 - r$ are the two energy bands, with $r = \sqrt{(t_{xx} - t_{zz})/2 + 4t_{xz}^2}$. In the numerical calculations, we use the effective hopping parameter $t = 0.28\text{ eV}$, which is somewhat smaller than predicted by first principle calculations, but can be justified when considering the correlated character of $\text{La}_4\text{Ni}_3\text{O}_{10}$, increasing the effective mass. We fix $\Delta_{\text{cf}} = t$, $\mu = -1.25t$, and the density $n = 4/3$.

The Raman vertices in the orbital basis are 2×2 matrices given by

$$R_{\mathbf{k}}^\gamma = \left(\frac{\partial^2}{\partial k_x^2} \pm \frac{\partial^2}{\partial k_y^2} \right) H_{\mathbf{k}} \quad (3)$$

where $+$ ($-$) corresponds to the $\gamma = A_{1g}$ (B_{1g}) vertex. Our model does not include second-nearest neighbor hopping t' , and therefore the B_{2g} vertex is not considered. Note that the B_{2g} Raman response is indeed significantly smaller than those in the A_{1g} and B_{1g} channels.

$$H_{DW} = \delta \sum_{\mathbf{k}} (x_{\mathbf{k}}^\dagger x_{\mathbf{k}+\mathbf{q}}^\dagger + z_{\mathbf{k}}^\dagger z_{\mathbf{k}+\mathbf{q}}^\dagger) + H.c. \quad (4)$$

where δ is the amplitude of the modulation of μ , and \mathbf{q} the ordering vector, mimicking a DW. We choose $\delta = 0.2t$ and $\mathbf{q} = (0, \pi)$, which is close to the nesting \mathbf{q} -vector.

In the presence of DW order, the Hamiltonian in the orbital basis is a 4×4 matrices given by

$$H = \begin{bmatrix} H_{\mathbf{k}} & \delta I \\ \delta I & H_{\mathbf{k}+\mathbf{q}} \end{bmatrix}, \quad (5)$$

where I is the 2×2 identity matrix.

The Hamiltonian in the band basis, $H_{\mathbf{k}}^B = U^\dagger H_{\mathbf{k}} U$, is obtained from the orbital basis via the rotation matrices U , and can be diagonalized to give four bands α with energies E_α .

The Raman vertices in the orbital basis, in first approximation, are (see Ref. 22)

$$R^\gamma = \begin{bmatrix} R_{\mathbf{k}}^\gamma & 0 \\ 0 & R_{\mathbf{k}+\mathbf{q}}^\gamma \end{bmatrix}. \quad (6)$$

Analogous to the Hamiltonian, the Raman vertices can be transformed from the orbital to the band basis via $R_B^\gamma = U^\dagger R^\gamma U$.

The Raman response is calculated as the imaginary part of the following expression

$$\chi^\gamma(i\omega_n) = \sum_{\mathbf{k}, i\nu_n} \text{Tr}[R_B^\gamma G(i\nu_n) R_B^\gamma G(i\nu_n + i\omega_n)] \quad (7)$$

after analytical continuation $i\omega_n = \omega + i\Gamma$. Here G is the quasiparticle part of the Green's function, i.e. we account for the Raman transitions between the coherent quasiparticle α bands. Due to correlations, an energy-dependent quasiparticle weight $Z(E) \propto \eta^2/(E^2 + \eta^2)$ with $\eta = 0.5t$ is introduced, leading to $G_\alpha(i\nu_n) = Z(E_\alpha)(i\nu_n - E_\alpha)^{-1}$,

where E_α are the eigenvalues of Eq. 5 and ν_n the fermionic Matsubara frequencies.

DATA AVAILABILITY

Data that support the findings of this study are available from the corresponding authors upon request.

REFERENCES

-
- [1] D. J. Scalapino, A common thread: The pairing interaction for unconventional superconductors, *Rev. Mod. Phys.* **84**, 1383 (2012).
 - [2] P. A. Lee, N. Nagaosa, and X.-G. Wen, Doping a mott insulator: Physics of high-temperature superconductivity, *Rev. Mod. Phys.* **78**, 17 (2006).
 - [3] R. M. Fernandes, A. I. Coldea, H. Ding, I. R. Fisher, P. J. Hirschfeld, and G. Kotliar, Iron pnictides and chalcogenides: a new paradigm for superconductivity, *Nature* **601**, 35–44 (2022).
 - [4] P. Gegenwart, Q. Si, and F. Steglich, Quantum criticality in heavy-fermion metals, *Nat. Phys.* **4**, 186 (2008).
 - [5] J. A. N. Bruin, H. Sakai, R. S. Perry, and A. P. Mackenzie, Similarity of Scattering Rates in Metals Showing T-Linear Resistivity, *Science* **339**, 804 (2013).
 - [6] T. Timusk and B. Statt, The pseudogap in high-temperature superconductors: an experimental survey, *Rep. Prog. Phys.* **62**, 61 (1999).
 - [7] B. Keimer, S. Kivelson, M. Norman, *et al.*, From quantum matter to high-temperature superconductivity in copper oxides, *Nature* **518**, 179 (2015).
 - [8] G. Ghiringhelli, M. L. Tacon, M. Minola, S. Blanco-Canosa, C. Mazzoli, N. B. Brookes, G. M. D. Luca, A. Frano, D. G. Hawthorn, F. He, T. Loew, M. M. Sala, D. C. Peets, M. Salluzzo, E. Schierle, R. Sutarto, G. A. Sawatzky, E. Weschke, B. Keimer, and L. Braicovich, Long-Range Incommensurate Charge Fluctuations in (Y,Nd)Ba₂Cu₃O_{6+x}, *Science* **337**, 821 (2012).
 - [9] R. J. Birgeneau, C. Stock, J. M. Tranquada, and K. Yamada, Magnetic neutron scattering in hole-doped cuprate superconductors, *J. Phys. Soc. Jpn.* **75**, 111003 (2006).
 - [10] P. Dai, Antiferromagnetic order and spin dynamics in iron-based superconductors, *Rev. Mod. Phys.* **87**, 855 (2015).
 - [11] A. Damascelli, Z. Hussain, and Z.-X. Shen, Angle-resolved photoemission studies of the cuprate superconductors, *Rev. Mod. Phys.* **75**, 473 (2003).
 - [12] J. Fink, M. Knupfer, S. Atzkern, and M. Golden, Electronic correlations in solids, studied using electron energy-loss spectroscopy, *J. Electron Spectros. Relat. Phenomena* **117–118**, 287 (2001).
 - [13] O. Fischer, M. Kugler, I. Maggio-Aprile, C. Berthod, and C. Renner, Scanning tunneling spectroscopy of high-temperature superconductors, *Rev. Mod. Phys.* **79**, 353 (2007).
 - [14] D. N. Basov and T. Timusk, Electrodynamics of high- T_c superconductors, *Rev. Mod. Phys.* **77**, 721 (2005).
 - [15] T. P. Devereaux and R. Hackl, Inelastic light scattering from correlated electrons, *Rev. Mod. Phys.* **79**, 175 (2007).
 - [16] M. Le Tacon, A. Sacuto, A. Georges, G. Kotliar, Y. Gallais, D. Colson, and A. Forget, Two energy scales and two distinct quasiparticle dynamics in the superconducting state of underdoped cuprates, *Nat. Phys.* **2**, 537 (2006).
 - [17] S. L. Cooper, F. Slakey, M. V. Klein, J. P. Rice, E. D. Bukowski, and D. M. Ginsberg, Gap anisotropy and phonon self-energy effects in single-crystal YBa₂Cu₃O_{7- δ} , *Phys. Rev. B* **38**, 11934 (1988).
 - [18] M. Opel, R. Nemetschek, C. Hoffmann, R. Philipp, P. F. Müller, R. Hackl, I. Tüttő, A. Erb, B. Revaz, E. Walker, H. Berger, and L. Forró, Carrier relaxation, pseudogap, and superconducting gap in high- T_c cuprates: A Raman scattering study, *Phys. Rev. B* **61**, 9752 (2000).
 - [19] M. Bakr, A. P. Schnyder, L. Klam, D. Manske, C. T. Lin, B. Keimer, M. Cardona, and C. Ulrich, Electronic and phononic Raman scattering in detwinned YBa₂Cu₃O_{6.95} and Y_{0.85}Ca_{0.15}Ba₂Cu₃O_{6.95}: s -wave admixture to the $d_{x^2-y^2}$ -wave order parameter, *Phys. Rev. B* **80**, 064505 (2009).
 - [20] Y. Gallais, R. M. Fernandes, I. Paul, L. Chauvière, Y.-X. Yang, M.-A. Méasson, M. Cazayous, A. Sacuto, D. Colson, and A. Forget, Observation of Incipient Charge Nematicity in Ba(Fe_{1-x}Co_x)₂As₂, *Phys. Rev. Lett.* **111**, 267001 (2013).
 - [21] F. Kretzschmar, T. Böhm, U. Karahasanović, B. Muschler, A. Baum, D. Jost, J. Schmalian, S. Caprara, M. Grilli, C. Di Castro, J. G. Analytis, J.-H. Chu, I. R. Fisher, and R. Hackl, Critical spin fluctuations and the origin of nematic order in Ba(Fe_{1-x}Co_x)₂As₂, *Nat. Phys.* **12**, 560 (2016).
 - [22] B. Loret, N. Auvray, Y. Gallais, *et al.*, Intimate link between charge density wave, pseudogap and superconducting energy scales in cuprates, *Nat. Phys.* **15**, 771 (2019).
 - [23] Y. Nomura and R. Arita, Superconductivity in infinite-layer nickelates, *Rep. Prog. Phys.* **85**, 052501 (2022).
 - [24] M. Wang, H.-H. Wen, T. Wu, D.-X. Yao, and T. Xiang, Normal and Superconducting Properties of La₃Ni₂O₇, *Chin. Phys. Lett.* **41**, 077402 (2024).
 - [25] H. Sun, M. Huo, X. Hu, *et al.*, Signatures of superconductivity near 80 K in a nickelate under high pressure, *Nature* **621**, 493 (2023).

- [26] F. Li, D. Peng, J. Dou, N. Guo, L. Ma, C. Liu, L. Wang, Y. Zhang, J. Luo, J. Yang, J. Zhang, W. Cai, J. Cheng, Q. Zheng, R. Zhou, Q. Zeng, X. Tao, and J. Zhang, Ambient pressure growth of bilayer nickelate single crystals with superconductivity over 90 K under high pressure, (2025), [arXiv:2501.14584](#).
- [27] Y. Zhu, D. Peng, E. Zhang, B. Pan, X. Chen, L. Chen, H. Ren, F. Liu, Y. Hao, N. Li, Z. Xing, F. Lan, J. Han, J. Wang, D. Jia, H. Wo, Y. Gu, Y. Gu, L. Ji, W. Wang, H. Gou, Y. Shen, T. Ying, X. Chen, W. Yang, H. Cao, C. Zheng, Q. Zeng, J.-g. Guo, and J. Zhao, Superconductivity in pressurized trilayer $\text{La}_4\text{Ni}_3\text{O}_{10-\delta}$ single crystals, *Nature* **631**, 531–536 (2024).
- [28] H. Sakakibara, M. Ochi, H. Nagata, Y. Ueki, H. Sakurai, R. Matsumoto, K. Terashima, K. Hirose, H. Ohta, M. Kato, Y. Takano, and K. Kuroki, Theoretical analysis on the possibility of superconductivity in the trilayer Ruddlesden-Popper nickelate $\text{La}_4\text{Ni}_3\text{O}_{10}$ under pressure and its experimental examination: Comparison with $\text{La}_3\text{Ni}_2\text{O}_7$, *Phys. Rev. B* **109**, 144511 (2024).
- [29] Q. Li, Y.-J. Zhang, Z.-N. Xiang, Y. Zhang, X. Zhu, and H.-H. Wen, Signature of superconductivity in pressurized $\text{La}_4\text{Ni}_3\text{O}_{10}$, *Chin. Phys. Lett.* **41**, 017401 (2024).
- [30] M. Zhang, C. Pei, D. Peng, X. Du, W. Hu, Y. Cao, Q. Wang, J. Wu, Y. Li, H. Liu, C. Wen, J. Song, Y. Zhao, C. Li, W. Cao, S. Zhu, Q. Zhang, N. Yu, P. Cheng, L. Zhang, Z. Li, J. Zhao, Y. Chen, C. Jin, H. Guo, C. Wu, F. Yang, Q. Zeng, S. Yan, L. Yang, and Y. Qi, Superconductivity in Trilayer Nickelate $\text{La}_4\text{Ni}_3\text{O}_{10}$ under Pressure, *Phys. Rev. X* **15**, 021005 (2025).
- [31] J. Zhang, D. Phelan, A. S. Botana, *et al.*, Intertwined density waves in a metallic nickelate, *Nat. Commun.* **11**, 6003 (2020).
- [32] M. Kakoi, T. Oi, Y. Ohshita, M. Yashima, K. Kuroki, T. Kato, H. Takahashi, S. Ishiwata, Y. Adachi, N. Hatada, T. Uda, and H. Mukuda, Multiband metallic ground state in multilayered nickelates $\text{La}_3\text{Ni}_2\text{O}_7$ and $\text{La}_4\text{Ni}_3\text{O}_{10}$ probed by ^{139}La -nmr at ambient pressure, *J. Phys. Soc. Jpn.* **93**, 053702 (2024).
- [33] M. Li, J. Gong, Y. Zhu, Z. Chen, J. Zhang, E. Zhang, Y. Li, R. Yin, S. Wang, J. Zhao, D.-L. Feng, Z. Du, and Y.-J. Yan, Direct Visualization of an Incommensurate Unidirectional Charge Density Wave in $\text{La}_4\text{Ni}_3\text{O}_{10}$, [arXiv:2501.18885](#) (2025).
- [34] R. Khasanov, T. J. Hicken, I. Plokhikh, V. Sazgari, L. Keller, V. Pomjakushin, M. Bartkowiak, S. Krolak, M. J. Winarski, J. A. Krieger, H. Luetkens, T. Klimczuk, D. J. Gawryluk, and Z. Guguchia, Identical Suppression of Spin and Charge Density Wave Transitions in $\text{La}_4\text{Ni}_3\text{O}_{10}$ by Pressure, [arXiv:2503.04400](#) (2025).
- [35] T. Fukamachi, K. Oda, Y. Kobayashi, T. Miyashita, and M. Sato, Studies on Successive Electronic State Changes in Systems with NiO_2 Planes – ^{139}La -NMR/NQR–, *J. Phys. Soc. Jpn.* **70**, 2757 (2001).
- [36] R. Khasanov, T. J. Hicken, D. J. Gawryluk, V. Sazgari, I. Plokhikh, L. P. Sorel, M. Bartkowiak, S. Bötzel, F. Lechermann, I. M. Eremin, H. Luetkens, and Z. Guguchia, Pressure-enhanced splitting of density wave transitions in $\text{La}_3\text{Ni}_2\text{O}_7$, *Nat. Phys.* **21**, 430 (2025).
- [37] C.-Q. Chen, Z. Luo, M. Wang, W. Wú, and D.-X. Yao, Trilayer multiorbital models of $\text{La}_4\text{Ni}_3\text{O}_{10}$, *Phys. Rev. B* **110**, 014503 (2024).
- [38] Q.-G. Yang, K.-Y. Jiang, D. Wang, H.-Y. Lu, and Q.-H. Wang, Effective model and s_{\pm} -wave superconductivity in trilayer nickelate $\text{La}_4\text{Ni}_3\text{O}_{10}$, *Phys. Rev. B* **109**, L220506 (2024).
- [39] Y. Zhang, L.-F. Lin, A. Moreo, T. A. Maier, and E. Dagotto, Prediction of s^{\pm} -Wave Superconductivity Enhanced by Electronic Doping in Trilayer Nickelates $\text{La}_4\text{Ni}_3\text{O}_{10}$ under Pressure, *Phys. Rev. Lett.* **133**, 136001 (2024).
- [40] J. Huang and T. Zhou, Interlayer pairing-induced partially gapped Fermi surface in trilayer $\text{La}_4\text{Ni}_3\text{O}_{10}$ superconductors, *Phys. Rev. B* **110**, L060506 (2024).
- [41] H. LaBollita, J. Kapeghian, M. R. Norman, and A. S. Botana, Electronic structure and magnetic tendencies of trilayer $\text{La}_4\text{Ni}_3\text{O}_{10}$ under pressure: Structural transition, molecular orbitals, and layer differentiation, *Phys. Rev. B* **109**, 195151 (2024).
- [42] I. V. Leonov, Electronic structure and magnetic correlations in the trilayer nickelate superconductor $\text{La}_4\text{Ni}_3\text{O}_{10}$ under pressure, *Phys. Rev. B* **109**, 235123 (2024).
- [43] Q. Qin, J. Wang, and Y. feng Yang, Frustrated superconductivity and intrinsic reduction of T_c in trilayer nickelate, *Innov. Mater.* **2**, 100102 (2024).
- [44] P.-F. Tian, H.-T. Ma, X. Ming, X.-J. Zheng, and H. Li, Effective model and electron correlations in trilayer nickelate superconductor $\text{La}_4\text{Ni}_3\text{O}_{10}$, *J. Phys.: Condens. Matter* **36**, 355602 (2024).
- [45] J.-X. Wang, Z. Ouyang, R.-Q. He, and Z.-Y. Lu, Non-Fermi liquid and Hund correlation in $\text{La}_4\text{Ni}_3\text{O}_{10}$ under high pressure, *Phys. Rev. B* **109**, 165140 (2024).
- [46] M. Zhang, H. Sun, Y.-B. Liu, Q. Liu, W.-Q. Chen, and F. Yang, s^{\pm} -wave superconductivity in pressurized $\text{La}_4\text{Ni}_3\text{O}_{10}$, *Phys. Rev. B* **110**, L180501 (2024).
- [47] M. Zhang, H. Sun, Y.-B. Liu, Q. Liu, W.-Q. Chen, and F. Yang, Spin-density wave and superconductivity in $\text{La}_4\text{Ni}_3\text{O}_{10}$ under ambient pressure, *Phys. Rev. B* **111**, 144502 (2025).
- [48] H. Li, X. Zhou, T. Nummy, J. Zhang, V. Pardo, W. E. Pickett, J. F. Mitchell, and D. S. Dessau, Fermiology and electron dynamics of trilayer nickelate $\text{La}_4\text{Ni}_3\text{O}_{10}$, *Nat. Commun.* **8**, 704 (2017).
- [49] X. Du, Y. D. Li, Y. T. Cao, C. Y. Pei, M. X. Zhang, W. X. Zhao, K. Y. Zhai, R. Z. Xu, Z. K. Liu, Z. W. Li, J. K. Zhao, G. Li, Y. L. Chen, Y. P. Qi, H. J. Guo, and L. X. Yang, Correlated Electronic Structure and Density-Wave Gap in Trilayer Nickelate $\text{La}_4\text{Ni}_3\text{O}_{10}$, [arxiv:2405.19853](#) (2024).
- [50] Y. Li, Y. Cao, L. Liu, P. Peng, H. Lin, C. Pei, M. Zhang, H. Wu, X. Du, W. Zhao, K. Zhai, X. Zhang, J. Zhao, M. Lin, P. Tan, Y. Qi, G. Li, H. Guo, L. Yang, and L. Yang, Distinct ultrafast dynamics of bilayer and trilayer nickelate superconductors regarding the density-wave-like transitions, *Sci. Bull.* **70**, 180 (2025).
- [51] S. Xu, C.-Q. Chen, M. Huo, D. Hu, H. Wang, Q. Wu, R. Li, D. Wu, M. Wang, D.-X. Yao, T. Dong, and N. Wang, Origin of the density wave instability in trilayer nickelate $\text{La}_4\text{Ni}_3\text{O}_{10}$ revealed by optical and ultrafast spectroscopy, *Phys. Rev. B* **111**, 075140 (2025).
- [52] S. Xu, H. Wang, M. Huo, D. Hu, Q. Wu, L. Yue, D. Wu, M. Wang, T. Dong, and N. Wang, Collapse of density wave and emergence of superconductivity in pressurized- $\text{La}_4\text{Ni}_3\text{O}_{10}$ evidenced by ultrafast spectroscopy, [arXiv:2503.05176](#) (2025).
- [53] D.-H. Gim, C. H. Park, and K. H. Kim, Orbital-selective quasiparticle depletion across the density wave transition in trilayer nickelate $\text{La}_4\text{Ni}_3\text{O}_{10}$, [arXiv:2505.05068](#)

- (2025).
- [54] C. Lu, Z. Pan, F. Yang, and C. Wu, Superconductivity in $\text{La}_4\text{Ni}_3\text{O}_{10}$ under pressure, *Phys. Rev. B* **111**, 134515 (2025).
 - [55] Y. Zhang, L.-F. Lin, A. Moreo, S. Okamoto, T. A. Maier, and E. Dagotto, General trends of electronic structures, superconducting pairing, and magnetic correlations in the Ruddlesden-Popper nickelate m -layered superconductors $\text{La}_{m+1}\text{Ni}_m\text{O}_{3m+1}$, [arXiv:2504.14327](#) (2025).
 - [56] Z. Luo, X. Hu, M. Wang, W. Wú, and D.-X. Yao, Bilayer Two-Orbital Model of $\text{La}_3\text{Ni}_2\text{O}_7$ under Pressure, *Phys. Rev. Lett.* **131**, 126001 (2023).
 - [57] F. Lechermann, J. Gondolf, S. Bötzel, and I. M. Eremin, Electronic correlations and superconducting instability in $\text{La}_3\text{Ni}_2\text{O}_7$ under high pressure, *Phys. Rev. B* **108**, L201121 (2023).
 - [58] V. Christiansson, F. Petocchi, and P. Werner, Correlated Electronic Structure of $\text{La}_3\text{Ni}_2\text{O}_7$ under Pressure, *Phys. Rev. Lett.* **131**, 206501 (2023).
 - [59] Y. Cao and Y.-f. Yang, Flat bands promoted by Hund's rule coupling in the candidate double-layer high-temperature superconductor $\text{La}_3\text{Ni}_2\text{O}_7$ under high pressure, *Phys. Rev. B* **109**, L081105 (2024).
 - [60] S. Ryee, N. Witt, G. Sangiovanni, and T. O. Wehling, Optimal superconductivity near a Lifshitz transition in strained $(\text{La},\text{Pr})_3\text{Ni}_2\text{O}_7$, (2025), [arXiv:2506.21480](#).
 - [61] X. Jia, Y. Shen, H. LaBollita, X. Chen, J. Zhang, Y. Li, H. Zhao, M. G. Kanatzidis, M. Krogstad, H. Zheng, A. Said, A. Alatas, S. Rosenkranz, D. Phelan, M. P. M. Dean, M. R. Norman, J. F. Mitchell, A. S. Botana, and Y. Cao, Lattice-charge coupling in a trilayer nickelate with intertwined density wave order, (2025), [arXiv:2507.13513](#).
 - [62] J. Zhang, H. Zheng, Y.-S. Chen, Y. Ren, M. Yonemura, A. Huq, and J. F. Mitchell, High oxygen pressure floating zone growth and crystal structure of the metallic nickelates $R_4\text{Ni}_3\text{O}_{10}$ ($R = \text{La}, \text{Pr}$), *Phys. Rev. Mater.* **4**, 083402 (2020).
 - [63] N. Yuan, A. Elghandour, J. Arneth, K. Dey, and R. Klingeler, High-pressure crystal growth and investigation of the metal-to-metal transition of Ruddlesden-Popper trilayer nickelates $\text{La}_4\text{Ni}_3\text{O}_{10}$, *J. Cryst. Growth* **627**, 127511 (2024).
 - [64] M. Shi, Y. Li, Y. Wang, D. Peng, S. Yang, H. Li, K. Fan, K. Jiang, J. He, Q. Zeng, D. Song, B. Ge, Z. Xiang, Z. Wang, J. Ying, T. Wu, and X. Chen, Absence of superconductivity and density-wave transition in ambient-pressure tetragonal $\text{La}_4\text{Ni}_3\text{O}_{10}$, *Nat. Commun.* **16**, 2887 (2025).
 - [65] N. Chaban, M. Weber, S. Pignard, and J. Kreisel, Phonon raman scattering of perovskite LaNiO_3 thin films, *Appl. Phys. Lett.* **97**, 031915 (2010).
 - [66] M. Hepting, M. Minola, A. Frano, G. Cristiani, G. Logvenov, E. Schierle, M. Wu, M. Bluschke, E. Weschke, H.-U. Habermeier, E. Benckiser, M. Le Tacon, and B. Keimer, Tunable Charge and Spin Order in PrNiO_3 Thin Films and Superlattices, *Phys. Rev. Lett.* **113**, 227206 (2014).
 - [67] L. Wang, H. Liu, V. Zimmermann, A. K. Yogi, M. Isobe, M. Minola, M. Hepting, G. Khaliullin, and B. Keimer, Spin-Orbit Excitons in a Correlated Metal: Raman Scattering Study of Sr_2RhO_4 , *Phys. Rev. Lett.* **132**, 116502 (2024).
 - [68] H. L. Liu, S. Yoon, S. L. Cooper, G. Cao, and J. E. Crow, Raman-scattering study of the charge and spin dynamics of the layered ruthenium oxide $\text{Ca}_3\text{Ru}_2\text{O}_7$, *Phys. Rev. B* **60**, R6980 (1999).
 - [69] S. Kumar, Øystein Fjellvåg, A. O. Sjøstad, and H. Fjellvåg, Physical properties of Ruddlesden-Popper ($n = 3$) nickelate: $\text{La}_4\text{Ni}_3\text{O}_{10}$, *J. Magn. Magn. Mater.* **496**, 165915 (2020).
 - [70] D. Rout, S. R. Mudi, M. Hoffmann, S. Spachmann, R. Klingeler, and S. Singh, Structural and physical properties of trilayer nickelates $R_4\text{Ni}_3\text{O}_{10}$ ($R = \text{La}, \text{Pr}$, and Nd), *Phys. Rev. B* **102**, 195144 (2020).
 - [71] C. Falter and F. Schnetgöke, Influence of ionic charge and dipole fluctuations on the lattice dynamics, dielectric properties, and infrared response of La_2CuO_4 , *Phys. Rev. B* **65**, 054510 (2002).
 - [72] T. C. Sterling and D. Reznik, Effect of the electronic charge gap on LO bond-stretching phonons in undoped La_2CuO_4 calculated using LDA + U, *Phys. Rev. B* **104**, 134311 (2021).
 - [73] Y. Gu, C. Le, Z. Yang, X. Wu, and J. Hu, Effective model and pairing tendency in bilayer Ni-based superconductor $\text{La}_3\text{Ni}_2\text{O}_7$ (2023), [arXiv:2306.07275](#).
 - [74] Z. Luo, X. Hu, M. Wang, W. Wú, and D.-X. Yao, Bilayer Two-Orbital Model of $\text{La}_3\text{Ni}_2\text{O}_7$ under Pressure, *Phys. Rev. Lett.* **131**, 126001 (2023).
 - [75] J. Shen, Y. Miao, Z. Ou, G. Zhou, Y. Chen, R. Luan, H. Sun, Z. Feng, X. Yong, P. Li, Y. Li, L. Xu, W. Lv, Z. Nie, H. Wang, H. Huang, Y.-J. Sun, Q.-K. Xue, Z. Chen, and J. He, Anomalous energy gap in superconducting $\text{La}_{2.85}\text{Pr}_{0.15}\text{Ni}_2\text{O}_7/\text{SrLaAlO}_4$ heterostructures, (2025), [arXiv:2502.17831](#).
 - [76] C. Le, J. Zhan, X. Wu, and J. Hu, Landscape of correlated orders in strained bilayer nickelate thin films, (2025), [arXiv:2501.14665](#).
 - [77] S. Deswal, D. Kumar, D. Rout, S. Singh, and P. Kumar, Dynamics of electron-electron correlated to electron-phonon coupled phase progression in trilayer nickelate $\text{La}_4\text{Ni}_3\text{O}_{10}$, (2024), [arXiv:2411.13933](#).
 - [78] X. Chen, J. Zhang, A. S. Thind, S. Sharma, H. LaBollita, G. Peterson, H. Zheng, D. P. Phelan, A. S. Botana, R. F. Klie, and J. F. Mitchell, Polymorphism in the Ruddlesden-Popper Nickelate $\text{La}_3\text{Ni}_2\text{O}_7$: Discovery of a Hidden Phase with Distinctive Layer Stacking, *J. Am. Chem. Soc.* **146**, 3640 (2024).
 - [79] P. Puphal, P. Reiss, N. Enderlein, Y.-M. Wu, G. Khaliullin, V. Sundaramurthy, T. Priessnitz, M. Knauff, A. Suthar, L. Richter, M. Isobe, P. A. van Aken, H. Takagi, B. Keimer, Y. E. Suyolcu, B. Wehinger, P. Hansmann, and M. Hepting, Unconventional Crystal Structure of the High-Pressure Superconductor $\text{La}_3\text{Ni}_2\text{O}_7$, *Phys. Rev. Lett.* **133**, 146002 (2024).
 - [80] J.-P. Pouget and E. Canadell, Structural approach to charge density waves in low-dimensional systems: electronic instability and chemical bonding, *Rep. Prog. Phys.* **87**, 026501 (2024).
 - [81] J. Zhan, Y. Gu, X. Wu, and J. Hu, Cooperation between Electron-Phonon Coupling and Electronic Interaction in Bilayer Nickelates $\text{La}_3\text{Ni}_2\text{O}_7$, *Phys. Rev. Lett.* **134**, 136002 (2025).
 - [82] C. Zhu, B. Li, Y. Fan, C. Yin, J. Zhai, J. Cheng, S. Liu, and Z. Shi, Magnetic phases and electron-phonon coupling in $\text{La}_3\text{Ni}_2\text{O}_7$ under pressure, *Comput. Mater. Sci.* **250**, 113676 (2025).

- [83] X.-W. Yi, Y. Meng, J.-W. Li, Z.-W. Liao, W. Li, J.-Y. You, B. Gu, and G. Su, Nature of charge density waves and metal-insulator transition in pressurized $\text{La}_3\text{Ni}_2\text{O}_7$, *Phys. Rev. B* **110**, L140508 (2024).
- [84] Z. Ouyang, M. Gao, and Z.-Y. Lu, Absence of electron-phonon coupling superconductivity in the bilayer phase of $\text{La}_3\text{Ni}_2\text{O}_7$ under pressure, *npj Quantum Mater.* **9**, 80 (2024).
- [85] Z. Liu, M. Huo, J. Li, Q. Li, Y. Liu, Y. Dai, X. Zhou, J. Hao, Y. Lu, M. Wang, and H.-H. Wen, Electronic correlations and partial gap in the bilayer nickelate $\text{La}_3\text{Ni}_2\text{O}_7$, *Nat. Commun.* **15** (2024).
- [86] T. Kondo, Y. Hamaya, A. D. Palczewski, T. Takeuchi, J. S. Wen, Z. J. Xu, G. Gu, J. Schmalian, and A. Kaminski, Disentangling cooper-pair formation above the transition temperature from the pseudogap state in the cuprates, *Nat. Phys.* **7**, 21 (2011).
- [87] M. Uchida, K. Ishizaka, P. Hansmann, Y. Kaneko, Y. Ishida, X. Yang, R. Kumai, A. Toschi, Y. Onose, R. Arita, K. Held, O. K. Andersen, S. Shin, and Y. Tokura, Pseudogap of Metallic Layered Nickelate $R_{2-x}\text{Sr}_x\text{NiO}_4$ ($R = \text{Nd, Eu}$) Crystals Measured Using Angle-Resolved Photoemission Spectroscopy, *Phys. Rev. Lett.* **106**, 027001 (2011).
- [88] M. R. Norman, Landau theory of the density wave transition in trilayer ruddlesden-popper nickelates, (2025), [arXiv:2506.07870](#).
- [89] Z. Liu, H. Sun, M. Huo, *et al.*, Evidence for charge and spin density waves in single crystals of $\text{La}_3\text{Ni}_2\text{O}_7$ and $\text{La}_3\text{Ni}_2\text{O}_6$, *Sci. China- Phys. Mech. Astron.* **66**, 217411 (2023).
- [90] Y.-Y. Zheng and W. Wú, s_{\pm} -wave superconductivity in the bilayer two-orbital Hubbard model, *Phys. Rev. B* **111**, 035108 (2025).
- [91] S. Fan, M. Ou, M. Scholten, Q. Li, Z. Shang, Y. Wang, J. Xu, H. Yang, I. M. Eremin, and H.-H. Wen, Superconducting gap structure and bosonic mode in $\text{La}_2\text{PrNi}_2\text{O}_7$ thin films at ambient pressure, (2025), [arXiv:2506.01788](#).
- [92] G. Kresse and J. Furthmüller, Efficient iterative schemes for ab initio total-energy calculations using a plane-wave basis set, *Phys. rev. B* **54**, 11169 (1996).
- [93] J. P. Perdew, K. Burke, and M. Ernzerhof, Generalized gradient approximation made simple, *Phys. Rev. Lett.* **77**, 3865 (1996).
- [94] G. Kresse and D. Joubert, From ultrasoft pseudopotentials to the projector augmented-wave method, *Phys. Rev. B* **59**, 1758 (1999).
- [95] S. Baroni, P. Giannozzi, and A. Testa, Green's-function approach to linear response in solids, *Phys. Rev. Lett.* **58**, 1861 (1987).
- [96] A. Togo, F. Oba, and I. Tanaka, First-principles calculations of the ferroelastic transition between rutile-type and CaCl_2 -type SiO_2 , at high pressures, *Phys. Rev. B* **78**, 134106 (2008).
- [97] A. Togo and I. Tanaka, First principles phonon calculations in materials science, *Scr. Mater.* **108**, 1 (2015).

ACKNOWLEDGMENTS

We thank Y. Gallais, G. Blesio, C. Falter, M. J. Graf von Westarp, and A. von Ungern-Sternberg Schwark for insightful discussions.